nature communications

Article

https://doi.org/10.1038/s41467-026-68429-w

Light-driven restructuring generates nanoisland NiIr alloy for efficient methane dry reforming

Received: 17 June 2025

Accepted: 5 January 2026

Chengxuan He[1,2], Ruijie Yang[1,2], Chenggui Zhong[1,2], Zhicheng Ye[1,2], Yuan Dong[1,2], Weihao Chen[1,2], Lingyun Chen[1,2], Zhihan Wang[1,2], Shiqun Wu[1,2] ✉ & Jinlong Zhang[1,2] ✉

The simultaneous utilization of methane and carbon dioxide via dry reforming holds promise for sustainable syngas production, yet conventional thermocatalytic processes suffer from energy-intensive operation and catalyst deactivation. Here, we report a light-driven methane dry reforming strategy utilizing sinter-resistant nano-island alloys catalyst, which are dynamically evolved from partially oxidized NiIr nanoclusters anchored on TiO_2 under photoexcitation. In situ characterization reveals interfacial charge oscillations on the catalyst induce a support-Ni-Ir electron transfer pathway, stabilizing oxidized Ni linkages while electronically modulating surface Ir sites. This dual functionality promotes CH_xO^* intermediate formation, suppressing coking during 100-h operation under intermittent illumination. By decoupling photoelectric and photothermal contributions, we demonstrate that localized photogenerated electrons dominate balanced syngas production, whereas photothermal effects enhance molecular vibrations. The optimized catalyst achieves a syngas rate of 10841 mmol g_{cat}^{-1} h^{-1} with 25.0% light-to-fuel efficiency, establishing a design paradigm for solar-driven alloy catalysts in greenhouse gas valorization.

Mitigating greenhouse gas emissions while securing sustainable routes for chemical energy conversion remains a central challenge in the transition toward a low-carbon future. Dry reforming of methane (DRM), which simultaneously converts methane (CH_4) and carbon dioxide (CO_2) into syngas (CO and H_2) as valuable chemical feedstocks, offers a promising pathway for greenhouse gas utilization[1,2]. Yet, the highly endothermic nature of DRM (CH_4 (g) + CO_2 (g) → 2CO (g) + $2H_2$ (g), $\Delta H^{o}_{298K} = +247.3$ kJ mol^{-1}) necessitates harsh operating conditions (typically 700–1000 °C) in conventional thermocatalysis. Such high temperatures consume substantial fossil fuels, undermining environmental benefits of CO_2 utilization[3–5]. In addition, the reverse water-gas shift (RWGS) reaction (CO_2 (g) + H_2 (g) → CO (g) + H_2O (g), $\Delta H^{o}_{298K} = +41.2$ kJ mol^{-1}), being thermodynamically favored under the high-temperature conditions, compromises syngas selectivity by lowering the H_2/CO ratio[6]. Solar light-driven catalysis has emerged as an energy-efficient alternative by synergistically combining photoelectric effects and photothermal heating to promote the dissociation of CH_4 and CO_2 without external heating[7–9].

In materials terms, noble metals as active sites display high intrinsic activity toward CH_4 and CO_2 activation but suffer from low atom efficiency and over-strong intermediate binding, often leading to side reactions[10]. Nickel-based catalysts are more economically viable and exhibit notable CH_4 activation capacity, which are prone to deactivation via carbon deposition[11]. Alloying noble metals with Ni modulates the electronic structure to optimize the balance between reactant activation and intermediate adsorption, thereby suppressing

---

[1]State Key Laboratory of Green Chemical Engineering and Industrial Catalysis, School of Chemistry and Molecular Engineering, East China University of Science and Technology, Shanghai, China. [2]Shanghai Engineering Research Center for Multi-media Environmental Catalysis and Resource Utilization, East China University of Science and Technology, Shanghai, China. ✉e-mail: wushiqun@ecust.edu.cn; jlzhang@ecust.edu.cn

side reactions and improving noble metal utilization efficiency. Moreover, ultrafine nanoclusters (<2 nm) could further enhance catalytic efficiency through maximized surface exposure and metal utilization[12,13]. However, stabilizing such clusters against aggregation under reaction conditions remains challenging. Recent studies[14–16] have demonstrated that integrating oxide nano-islands at metal-support interfaces can effectively suppress sintering through strong charge-mediated interactions. For instance, anchoring Pt[14] or Pd[16] on CeO_x nano-islands has been shown to spatially confine metal mobility. However, extending this nano-island strategy to ultrafine alloy architectures requiring both interfacial stabilization and electronic tuning has yet to be reported.

In addition, catalyst structural stability at the atomic scale under intense light irradiation and elevated temperatures, which are conditions inherent to photothermal catalysis, remains challenging for elucidating catalytic mechanisms. Whether such conditions preserve the active phase or drive transformations from metastable intermediates to thermodynamically favored structures is still poorly understood. Beyond thermal vibrations that commonly induce surface reconstruction at high temperatures, photoexcitation can trigger substantial charge redistribution between the support and active site[17–20]. This photoinduced charge transfer may alter the electronic structure of surface chemical bonds, reducing bond energies and promoting dynamic surface reconstruction[21,22]. Despite growing interest, elucidating the nature and formation of the active phase under photothermal conditions as well as disentangling the respective roles of photoelectric and photothermal effects in light-driven DRM, remains a critical yet unresolved challenge, limiting progress toward rational catalyst design.

In this work, we demonstrate that photoinduced interfacial charge oscillations in $NiIr/TiO_2$ trigger dynamic structural reconstruction into TiO_2-supported NiIr nano-island alloys stabilized by oxidized Ni linkages ($NiIr/TiO_2$-L_{Ni}). This structural evolution arises from accelerated electron transfer across the support-Ni-Ir interface under light excitation. The spatially and electronically synergistic configuration promotes CH_xO^* intermediate formation, effectively mitigates carbon deposition, and maintains stable performance for 100 h under intermittent illumination. Mechanistic investigations reveal that photoelectric effects dominate the reaction, contributing 57.5% of the syngas production rate and 91.7% of the H_2/CO ratio by facilitating C-H/C = O scission and H-H coupling, while photothermal effects enhance molecular vibrations and reactant diffusion. Under full feed gas flow, $NiIr/TiO_2$-L_{Ni} achieves a syngas production rate of 10841 mmol g_{cat}^{-1} h^{-1}, with a light-to-fuel efficiency (LTFE) of 25.0% and a turnover frequency (TOF) of 23 s^{-1}.

Results

Synthesis and atomic-scale structural analysis of partially oxidized NiIr nanoclusters on TiO_2

To construct bimetallic NiIr nanoclusters on TiO_2 with precise atomic pairing, we adopted a directional adsorption strategy[23] (Fig. 1a; see Methods for synthesis details). This approach leverages sequential electrostatic adsorption of cationic Ni complexes and anionic Ir precursors onto alkalized TiO_2 nanosheets, ensuring preferential Ir anchoring onto pre-adsorbed Ni sites. For the Ir precursor, we used a species complexed with quaternary ammonium cations to enable its phase transfer into an aprotic solvent. This controlled process prevents Ir ripening and leaching. Consequently, by conducting adsorption in this manner, we minimized competitive adsorption of Ni and Ir, effectively overcoming a key limitation of conventional co-impregnation methods. Subsequent H_2 calcination eliminated organic ligands while strengthening Ni-Ir metallic interactions, yielding ultrafine bimetallic clusters with uniform dispersion on the TiO_2 support (Fig. 1b). Inductively coupled plasma-atomic emission spectrometry (ICP-AES) confirms controlled metal loadings across $NiIr_x/TiO_2$ samples (Supplementary Fig. 1 and Table S1), where x denotes the Ir/Ni theoretical atomic ratio. The sublinear increase in Ir/Ni ratios with x suggests saturation of Ir adsorption onto pre-adsorbed Ni sites, excluding independent Ir deposition. For comparison, monometallic Ni/TiO_2 and Ir/TiO_2 were prepared with a theoretical loading of 1 wt% for each metal. Aberration-corrected high-angle annular dark-field scanning transmission electron microscopy (HAADF-STEM) analysis revealed that Ni species or Ir species on TiO_2 exhibited sub-1.2 nm clusters (Supplementary Figs. 2–3), whereas the $NiIr_x$ nanoclusters on TiO_2 showed an increase in size, progressively reaching up to 1.61 nm with higher Ir content (Supplementary Figs. 4). This trend supports the co-stabilization of Ni and Ir atoms within the bimetallic clusters. This size evolution directly supports the formation of bimetallic NiIr nanoclusters, as the incorporation of Ir stabilizes the clusters and promotes their growth. Atomic-scale characterization of $NiIr_{0.5}/TiO_2$ provided further insights into the spatial distribution of Ni and Ir atoms. Filtered and color-coded HAADF-STEM images and the corresponding intensity profiles (Fig. 1c, d, Supplementary Fig. 5b, c) revealed intertwined Ni-Ir distributions within individual clusters. The 3D surface plot of a selected region (Fig. 1f) highlighted Ir atoms (whitish-yellow peaks within blue dashed marks) surrounding Ni atoms (darker yellow bumps), demonstrating cohesive bimetallic nanocluster formation. Conversely, monometallic samples exhibited only metal-TiO_2 contrast (Supplementary Figs. 2g-h, 3e-f). Moreover, EDS line scans (Fig.1g) and elemental mapping (Fig. 1h and Supplementary Fig. 5d-i) confirmed the intimate contact between Ni and Ir atoms. Owing to the higher atomic ratio of Ni to Ir, trace amounts of isolated Ni species inevitably persist. Crucially, all Ir atoms preferentially occupy Ni-associated sites, with no detectable isolated Ir single atoms observed on the TiO_2 support (Fig. 1b).

Next, we elucidate the chemical structure and coordination environment of the NiIr nanoclusters. X-ray diffraction (XRD) patterns confirm exclusive anatase-phase TiO_2 (Supplementary Fig. 6), with no detectable reflections from metallic Ni or Ir phases, consistent with HAADF-STEM evidence of dispersed sub-2 nm clusters. Normalized Ir L_3-edge and Ni K-edge X-ray absorption near-edge spectroscopy (XANES) analysis reveal partially oxidized states of Ni and Ir (Supplementary Fig. 7a, b). Linear combination fitting (Supplementary Fig. 7c-d) shows higher Ir oxidation in Ir/TiO_2 (+3.6) than $NiIr_{0.5}/TiO_2$ (+2.7), and more reduced Ni in Ni/TiO_2 (+1.6) versus $NiIr_{0.5}/TiO_2$ (+1.8), indicating electron transfer from Ni to Ir, later corroborated by in situ analyses. Extended X-ray absorption fine structure (EXAFS) at the Ir L_3-edge provides atomic-scale coordination details (Fig. 1i). All samples exhibit a prominent peak at ~1.60 Å and a relatively weaker peak at ~2.56 Å, corresponding to Ir-O scattering and Ir-Ir scattering, respectively. Notably, $NiIr_x/TiO_2$ samples exhibit an additional peak at 2.18 Å, which can be attributed to Ni-Ir scattering. These results demonstrate that NiIr nanoclusters exhibit a partially oxidized state, with electronic modulation between Ni and Ir atoms. The partial oxidation probably arises from the interface reconstruction between nanocluster and the surface lattice O atoms of TiO_2 during the calcination process and the exposure to air during storage. This electronic structure, coupled with their ultrafine size, positions these partially oxidized NiIr nanoclusters (O_x-NiIr) as promising candidates for the adsorption of CH_4 and CO_2 due to their inherent thermal instability[19].

In situ CO probe molecule diffuse reflectance infrared fourier transform spectroscopy (DRIFTS) analyses were conducted to unravel the surface structure and adsorption behavior of NiIr nanoclusters (Supplementary Fig. 8 and Fig. 1j). Ni/TiO_2 exhibited negligible *CO chemisorption signals (<2100 cm^{-1}), which vanished entirely upon heating to 100 °C. This confirms the inadequacy of individual Ni sites for CO adsorption. In contrast, Ir-containing samples ($NiIr_x/TiO_2$, Ir/TiO_2) display intense *CO chemisorption bands (2100–1990 cm^{-1}), with adsorption strength scaling with Ir content. Heating-up desorption

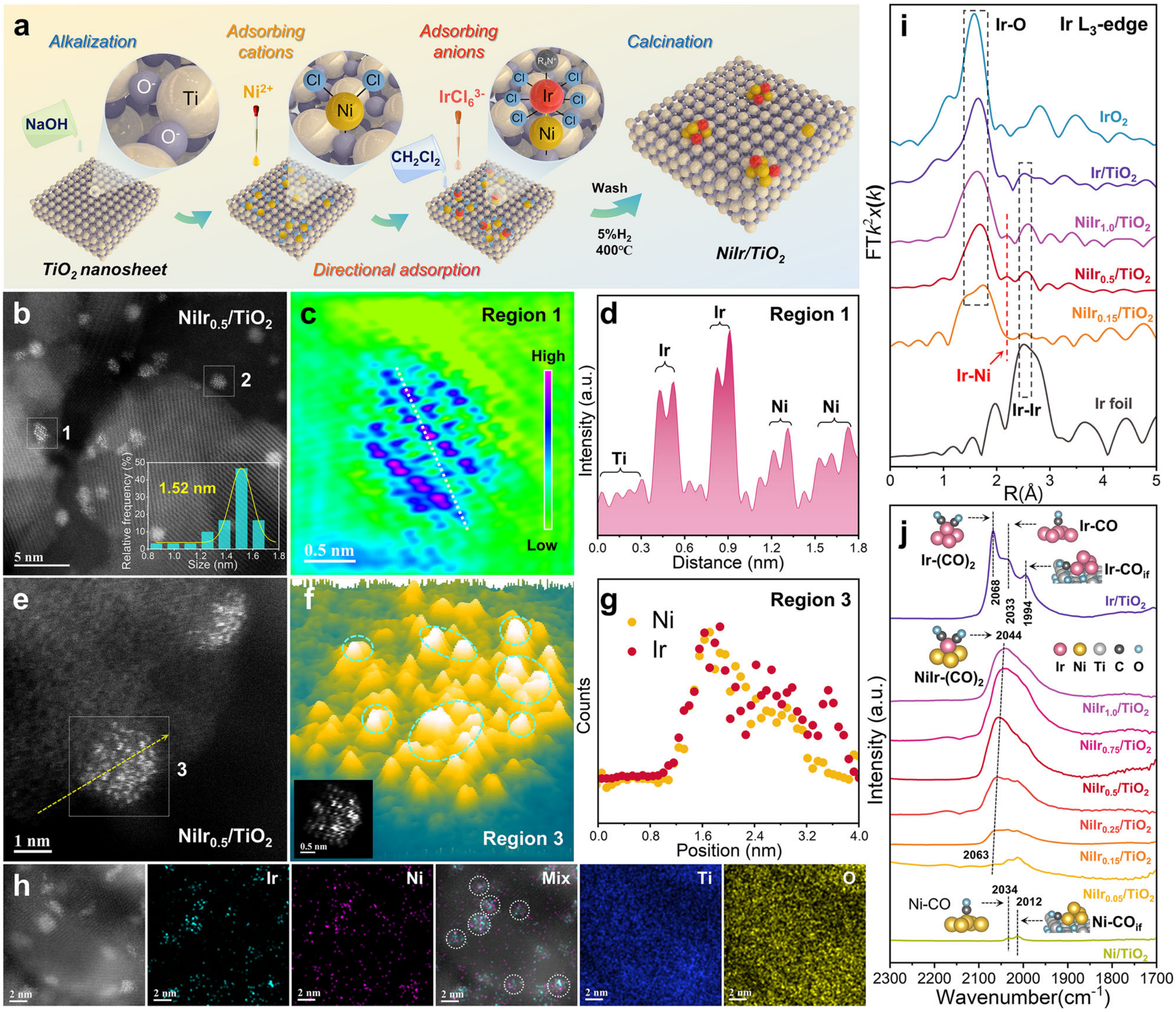

Fig. 1 | Synthesis and structural characterization of TiO_2-supported partially oxidized NiIr nanoclusters. **a** Schematic of the directional adsorption strategy for synthesizing NiIr nanoclusters supported on TiO_2. **b** Aberration-corrected HAADF-STEM image of $NiIr_{0.5}/TiO_2$ and cluster size distribution (inset). **c** Color-coded atomic map of region 1 (marked by the white dashed box in **b** after image filtering. **d** Intensity profiles along the white line in **c**. **e** Aberration-corrected HAADF-STEM image of NiIr nanoclusters on TiO_2. **f** 3D surface plot with atomic overlapping region 3 in **e**. Blue dashed circles indicate the Ir atoms in NiIr nanocluster. Inset: Filtered image of region 3. **g** EDS line-scan profiles of Ni and Ir across a cluster along the yellow arrow in **e**. **h** HAADF-STEM image and corresponding EDS elemental mapping of $NiIr_{0.5}/TiO_2$. **i** k^2-weighted Fourier transform of Ir L_3-edge EXAFS spectra (without phase correction) for Ir foil, IrO_2, $NiIr_x/TiO_2$, and Ir/TiO_2. **j** In situ CO-probe DRIFTS spectra of $NiIr_x/TiO_2$, Ni/TiO_2, and Ir/TiO_2 at the 15th min of Ar-flow during desorption (25 °C); schematic models of surface structures are included in **j**.

revealed a volcanic trend: *CO intensity peaked at 200 °C and declined continuously to 400 °C. It demonstrates reversible CO binding, which is a critical feature for sustaining DRM activity. Detailed comparison of the desorption spectra at 25 °C (Fig. 1j) highlights distinct Ir coordination environments. For Ir/TiO_2, three CO species were resolved: (i) multi-carbonyl Ir-$(CO)_2$ (2068 cm^{-1}, low-coordination sites)[24], (ii) linear CO on metallic Ir (Ir-CO, 2033 cm^{-1})[25], and (iii) bridged CO at Ir-TiO_2 interfaces (Ir_{if}-CO, 1994 cm^{-1})[26]. For Ni/TiO_2, only weak peaks of Ni-CO and Ni_{if}-CO can be observed. In $NiIr_x/TiO_2$, the dominant Ir-$(CO)_2$ peak progressively shifts downward (2063 → 2044 cm^{-1}) with increasing Ir content, signaling enhanced π-backdonation from Ir to CO. The observed redshift arises from Ni-to-Ir electron transfer, which elevates Ir's d-orbital occupancy, strengthens Ir-C bonds, and weakens C-O bonds. These results confirm that in partially oxidized NiIr nanoclusters, Ir serves as the main center for CO adsorption, while Ni modulates Ir's electronic properties to optimize the balance between adsorption strength and desorption kinetics.

Photoelectric-photothermal synergy in light-driven dry reforming of methane over $NiIr/TiO_2$

Light-driven DRM over TiO_2-supported NiIr nanoclusters was investigated under full-spectrum irradiation (Supplementary Fig. 9). Ni and Ir modification significantly enhanced DRM activity compared to pure TiO_2 (Fig. 2a, Supplementary Fig. 10). $NiIr_{0.5}/TiO_2$ achieved optimal performance (Fig. 2a, Supplementary Fig. 11 and Note 1) with syngas generation rates of 2512 mmol g_{cat}^{-1} h^{-1} and feed gas conversions near 60% at the condition of CH_4: CO_2: Ar =1: 1: 8. Increasing the Ir/Ni ratio (x) from 0.05 to 1.0 elevated H_2/CO from 0.68 to 1.03, demonstrating Ir-Ni synergy in balancing CH_4-CO_2 activation (Fig. 2a). $NiIr_{0.15}/TiO_2$ (equivalent Ir loading to 0.5% Ir/TiO_2) exhibited 2.13-fold higher activity (CH_4 conversion: 17% → 42%), underscoring the critical role of bimetallic interactions. Highly diluted conditions (CH_4: CO_2: Ar =1: 1: 98) achieved 90% conversion (Fig. 2b). Strikingly, at undiluted feed gas, the system achieved syngas generation rates of 10841 mmol g_{cat}^{-1} h^{-1}, with a LTFE of 25.0% and a TOF of 23 s^{-1}. However, for gas

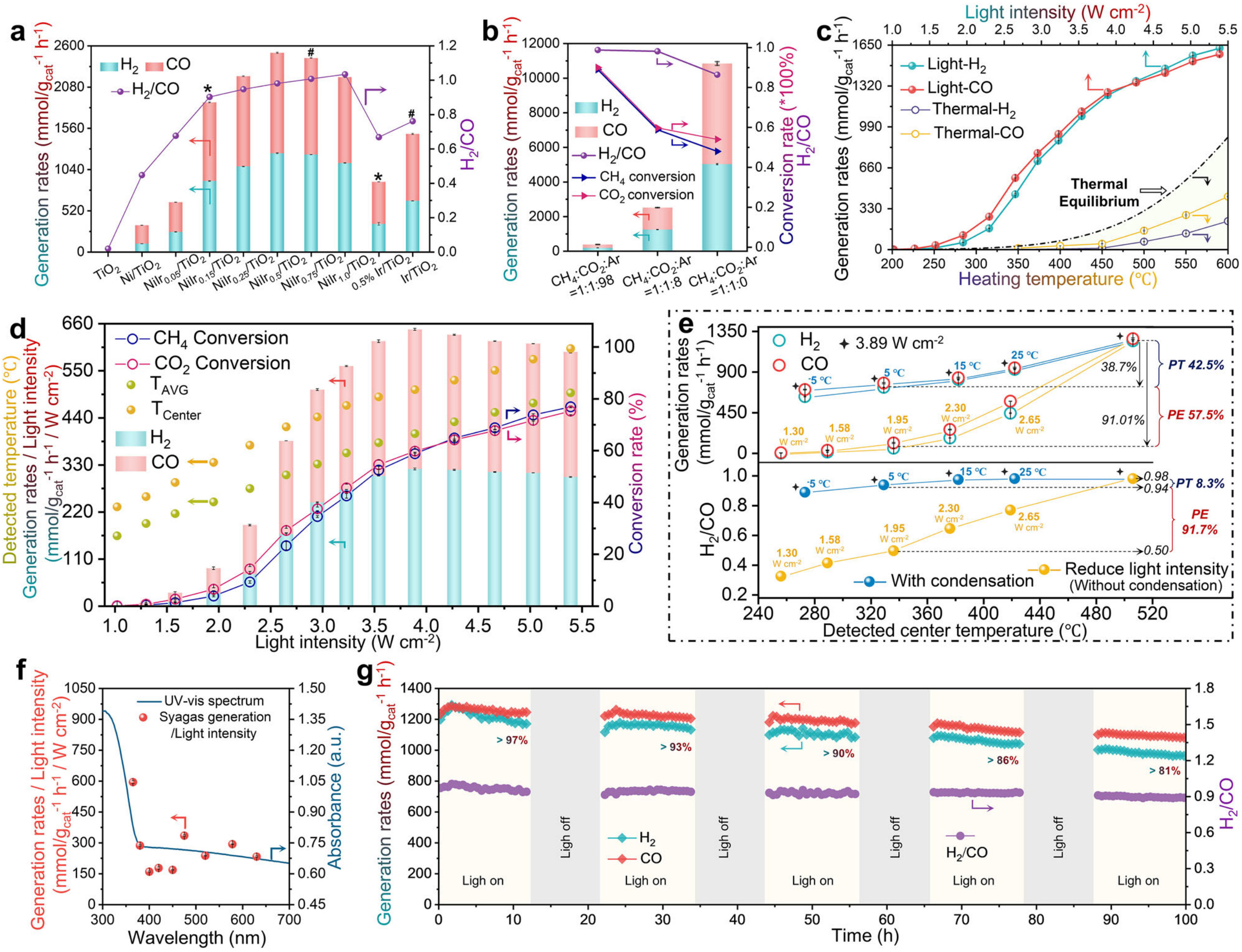

Fig. 2 | Light-driven dry reforming of methane performance of NiIr/TiO$_2$. **a** Syngas generation rates and H_2/CO ratios of TiO$_2$, Ni/TiO$_2$, Ir/TiO$_2$, and NiIr$_x$/TiO$_2$ under 3.89 W cm^{-2} light irradiation (feed gas: CH_4: CO_2: Ar =1: 1: 8). Note: the same * or # marks indicate that the actual Ir loading amounts of the two samples are similar. **b** Feed-gas composition dependence of syngas generation rates, H_2/CO ratios, and conversion rates for NiIr$_{0.5}$/TiO$_2$ (light intensity: 3.89 W cm^{-2}). **c** Syngas generation rates of NiIr$_{0.5}$/TiO$_2$ under light irradiation or external heating. (CH_4:CO_2:Ar =1:1:8, the heating temperature is near to the detected light irradiation temperature at catalyst center.) **d** DRM activity per-unit light intensity, detected temperatures, and conversion rates of NiIr$_{0.5}$/TiO$_2$ under varied light intensities (CH_4:CO_2:Ar =1:1:8). Note that the T_{AVG} and T_{Center} indicate the average and the center temperature of catalyst surface measured by a thermocouple, which agree with the results from the IR camera (Supplementary Fig. 13). **e** Syngas generation rates and H_2/CO ratio of NiIr$_{0.5}$/TiO$_2$ with (blue lines) or without (yellow lines) condensation equipment. (CH_4: CO_2: Ar =1: 1: 8, condensate temperatures noted in blue font) Note that the PT and PE represent photothermal contribution and photoelectric contribution, respectively. **f** UV-Vis-NIR spectrum and wavelength-dependent DRM activity (per W cm^{-2}) of NiIr$_{0.5}$/TiO$_2$ under monochromatic light (with 500 °C external heating, CH_4: CO_2: Ar =1: 1: 8). **g** 100-hour stability of NiIr$_{0.5}$/TiO$_2$ under light on/off cycles (Light on: 3.89 W cm^{-2}, CH_4: CO_2: Ar =1: 1: 8; Light off: exposed to air). Reaction conditions for a-g: 5 mg catalyst, flow rate = 20 ml min^{-1}; The error bars indicate that there were at least three independent tests.

conservation and safety considerations, subsequent tests were conducted using a feed gas mixture of CH_4: CO_2: Ar =1: 1: 8. Light irradiation dramatically reduced the apparent activation energies for CO and H_2 production to 35.33 and 44.65 kJ mol^{-1}, respectively, which is less than half those of thermal catalysis (68.76 and 99.19 kJ mol^{-1}), effectively breaking the limitation of thermal catalysis (Fig. 2c, Supplementary Fig. 12).

Activity surged above a threshold light intensity of 2 W cm^{-2}, marking the onset of photoelectric-photothermal synergy (Fig. 2d and Supplementary Fig. 13). Specifically, at lower intensities (<1.95 W cm^{-2}, T_{Center} < 336 °C), the observed activity originated predominantly from photoelectric effects. This assignment is confirmed by the sustained syngas production under illumination, which stands in clear contrast to the negligible activity observed in dark thermal catalysis experiments conducted below the 350 °C threshold (as shown in Fig. 2c and Supplementary Fig. 12a). The interplay between photothermal and photoelectric contributions peaked at 3.89 W cm^{-2} (T_{Center} = 506 °C; T_{AVG} = 403 °C). Beyond 4.27 W cm^{-2}, the system approached a state of photon absorption saturation. At this point, the catalyst could no longer utilize the additional photons for charge carrier generation, and consequently, the excess energy was redirected into thermal pathways. This mechanistic shift is evidenced by a distinct decline in the per-unit-light efficiency (syngas generation rates/light intensity), which occurred despite the continued rise in the catalyst temperature (T_{Center} exceeding 600 °C). This nonlinear response highlights the delicate balance between photocarriers generation and thermal dissipation in light-driven systems.

Controlled condensation experiments (Fig. 2e) decoupled photothermal and photoelectric effects by selectively suppressing thermal contributions. The blue trend line maintained constant light intensity (3.89 W cm^{-2}) to preserve the photoelectric effect and used condensation cooling to suppress photothermal contributions, while the yellow trend line varied light intensity (from 3.89 to 1.30 cm^{-2}) without condensation and diminished both effects simultaneously. By comparing the syngas production rates and H_2/CO ratios from these two paths at matched catalyst surface temperatures, it was determined that the photoelectric-dominated system (with condensation) contributed 57.5% to syngas rates and 91.7% to H_2/CO balance, compared to the photothermal-assisted system (without condensation). This contrast confirms that photogenerated carriers preferentially drive H-H coupling and carbon intermediate oxidation, while thermal energy primarily enhances vibration and mobility of reactants. Comparative tests on $NiIr_{0.5}/TiO_2$ and $NiIr_{0.5}/SiO_2$ (Supplementary Fig. 14 and Note 2) further confirmed that TiO_2-supported NiIr nanoclusters uniquely harness coupled photothermal-photoelectric effects to achieve efficient and stable DRM catalysis.

The UV-Vis-NIR spectra (Supplementary Fig. 15) revealed that the introduction of Ni and Ir significantly enhanced broadband light absorption across the entire spectral range compared to TiO_2. Crucially, the absorption profile across the full spectral range of $NiIr_{0.5}/TiO_2$ exhibited a strong correlation with the wavelength-dependent DRM activity (Fig. 2f), confirming that the reaction is primarily driven by photoexcitation rather than thermal effects and evidencing its light-driven nature. Long-term stability tests (Supplementary Fig. 16 and Note 3) demonstrated considerable durability as $NiIr_{0.5}/TiO_2$ retained >97% activity over 720 min under light, with near-unity carbon balance. In contrast, thermal catalysis at 500 °C suffered a 20% activity drop and significant carbon deposition, emphasizing light's role in suppressing deactivation. Moreover, $NiIr/TiO_2$ sustained 100-hour stability under 20% reactant flow during five light/dark cycles (Fig. 2g), retaining >80% syngas generation rates with $H_2/CO > 0.9$ throughout the test. Monometallic controls (Supplementary Fig. 17) further validated Ni-Ir synergy that Ni/TiO_2 rapidly deactivated due to CH_x accumulation, while Ir/TiO_2 maintained 70% stability over 720 min but exhibited suppressed H_2/CO ratios, probably due to RWGS side reaction.

These results reveal that UV-Vis- induced hot electrons at the NiIr-TiO_2 interface, consistent with ultrafast (<10 fs) UV photoinduced electrons in TiO_2[27], collaboratively cleave C-H/C = O bonds and mediate H-H coupling. Meanwhile, infrared absorption enhances local temperatures. This photoelectric-photothermal synergy suppresses carbon deposition and stabilizes active sites, achieving DRM efficiency in photothermal and even certain thermal systems (Supplementary Table 3)[7–9,28–40].

Light-induced dynamic restructuring to form NiIr nano-island alloy on TiO_2

Alloy structural evolution under operando light conditions is critical to unraveling true catalytic mechanisms, which was therefore systematically investigated. In situ X-ray absorption spectroscopy (XAS) and near-ambient pressure XPS (NAP-XPS) analyses revealed the light-induced structural reorganization of NiIr nanoclusters. Under light irradiation, Ir L_3-edge EXAFS spectra of $NiIr_{0.5}/TiO_2$ (Fig. 3a) show a dominant Ir-Ni scattering peak at 2.18 Å, replacing the initial Ir-O coordination observed in the dark. Concurrently, Ni K-edge EXAFS of $NiIr_{0.5}/TiO_2$ (Fig. 3b) retains Ni-O (1.60 Å) and Ni-Ni (2.09 Å) scattering alongside emerging Ni-Ir (2.18 Å) coordination, indicating alloy formation without complete Ni reduction. In contrast, monometallic Ni/TiO_2 under identical conditions transitions fully to metallic Ni-Ni bonds, while Ir/TiO_2 retains residual Ir-O coordination (Supplementary Fig. 18). This indicates that during the dynamic alloy formation under light, electrons are transferred from Ni to Ir. Quantitative EXAFS fitting analysis (Fig. 3c, Supplementary Fig. 19–20, Supplementary Tables 4–5) quantifies this structural evolution. Under light irradiation, $NiIr_{0.5}/TiO_2$ exhibits nearly 100% Ir-Ni coordination at the Ir L_3-edge and 32% Ir-Ni coordination at the Ni K-edge, alongside 37% Ni-O interfacial bonds. This contrasts sharply with monometallic Ni/TiO_2. The nearly 100% Ni-Ni coordination in Ni/TiO_2 likely drives its rapid deactivation (Supplementary Fig. 18), as non-oxidized Ni sites exhibit diminished ability to activate CH_4 and oxidize carbonaceous intermediates, leading to CH_x accumulation and irreversible poisoning. The absence of Ir-O coordination in $NiIr_{0.5}/TiO_2$ under light confirms that Ir in the alloy phase does not directly interact with TiO_2, while Ni maintains interfacial Ni-O bonds, forming a nano-island architecture that isolates the NiIr alloy from the support (Supplementary Fig. 21). This structure formation is critical for efficient and stable DRM catalysis.

In situ NAP-XPS analyses corroborate the XAS findings. To decouple photochemical and photothermal contributions, we first monitored structural evolution under unfocused light. The Ir 4*f* spectra (Fig. 3d) reveal a pronounced shift toward lower binding energy, with the Ir^0 fraction increasing from 36.96% (dark) to 60.65%. Upon switching to focused light, the Ir^0 fraction further rises to 62.31%. Figure 3e quantifies this trend: the $Ir^0/Ir^{\delta+}$ ratio increases by 0.95 under unfocused light, with only an additional 0.11 gain under focused irradiation, demonstrating that low-intensity light suffices to initiate alloying. Monometallic Ir/TiO_2 exhibits a smaller $Ir^0/Ir^{\delta+}$ increase of 0.61 under unfocused light (Supplementary Fig. 22), aligning with its higher oxidation state observed in in situ XAS. Moreover, air exposure restores the initial oxidized state (Fig. 3e, Supplementary Figs. 22–23), confirming the reversibility of the NiIr-L_{Ni} phase. Parallel in situ Ni 2*p* NAP-XPS (Supplementary Fig. 24a-c) shows analogous trends, with Ni^0/Ni^{2+} ratios tracking Ir's redox dynamics. While Ti 2*p* and O 1*s* exhibit the positive shift in the binding energy of Ti and $O_{Lattice}$ under light irradiation (Supplementary Fig. 24d-e), this demonstrates that electrons migrate from the TiO_2 support to Ni-Ir under illumination. Post-reaction characterizations (Supplementary Figs. 25–26) reveal that prolonged light-driven DRM preserves Ni-Ir intimacy. Re-oxidation in post-EXAFS (Supplementary Fig. 27 and Note 4) and reversible NAP-XPS trends confirm that $NiIr/TiO_2$-L_{Ni} exists transiently only under light irradiation. Thermal catalysis induces limited Ni or Ir reduction ($Ir^0/Ir^{\delta+}$=0.61 at 500 °C vs. 1.54 under unfocused light) and fails to form obvious Ni-Ir bonds (Supplementary Figs. 28–29), resulting in poor DRM performance. Conversely, light irradiation in pure Ar still forms dominant Ni-Ir scattering (Supplementary Figs. 30–31 and Note 5), proving that reactant gases are non-essential for NiIr alloying. Moreover, light cessation triggers rapid re-oxidation, with full structural recovery after air exposure.

Figure 3f illustrates the light-induced structural dynamics in $NiIr/TiO_2$. Initial O_x-$NiIr/TiO_2$ adsorbs CH_4/CO_2 but remains inefficient and prone to coking. Under light irradiation, interfacial oscillations drive electrons from Ni to Ir, and Ir atoms migrate away from the interface, forming NiIr island alloy anchored via oxidized Ni linkages on TiO_2. The Ir-Ni binary phase diagram (Supplementary Fig. 32) and positive segregation energy (0.23 eV)[41] confirm alloy feasibility under photoexcitation. We further constructed DFT structures (Supplementary Fig. 33) for a series of samples based on the above analysis and actual Ni/Ir atomic ratios. Figure 3g confirms $NiIr/TiO_2$-L_{Ni}'s stability with a lower formation energy than the hypothetical Ir-linked model ($NiIr/TiO_2$-L_{Ir}), where Ir-O bonds elongate (black arrow indication, >3.0 Å), destabilizing the interface. These results demonstrate that light excitation dynamically restructures O_x-$NiIr/TiO_2$ into $NiIr/TiO_2$-L_{Ni}. The reversibility of $NiIr/TiO_2$-L_{Ni} under ambient conditions highlights its transient, light-governed property, serving as a suitable model for further investigation of photoelectric-dominated reaction mechanisms.

It is worth elucidating that the light-induced surface restructuring observed in this study is supported by prior findings regarding bimetallic systems. It is established that electron transfer in bimetallic clusters can drive surface segregation of one of the metals[42,43]. A pertinent mechanism involves atomic size, in which the introduction of a larger-radius atom (e.g., Sn in PtCu) can promote surface extraction and alloy reorganization[21,44]. In our system, Ir has a larger inherent atomic radius than Ni. Critically, the light-induced electron transfer from Ni to Ir reduces Ir's oxidation state, further exacerbating this radius disparity ($Ir^0 > Ir^{\delta+} > Ni^{\delta+}$) and thereby strongly promoting the surface exposure of Ir. This process is further enabled by the photo-

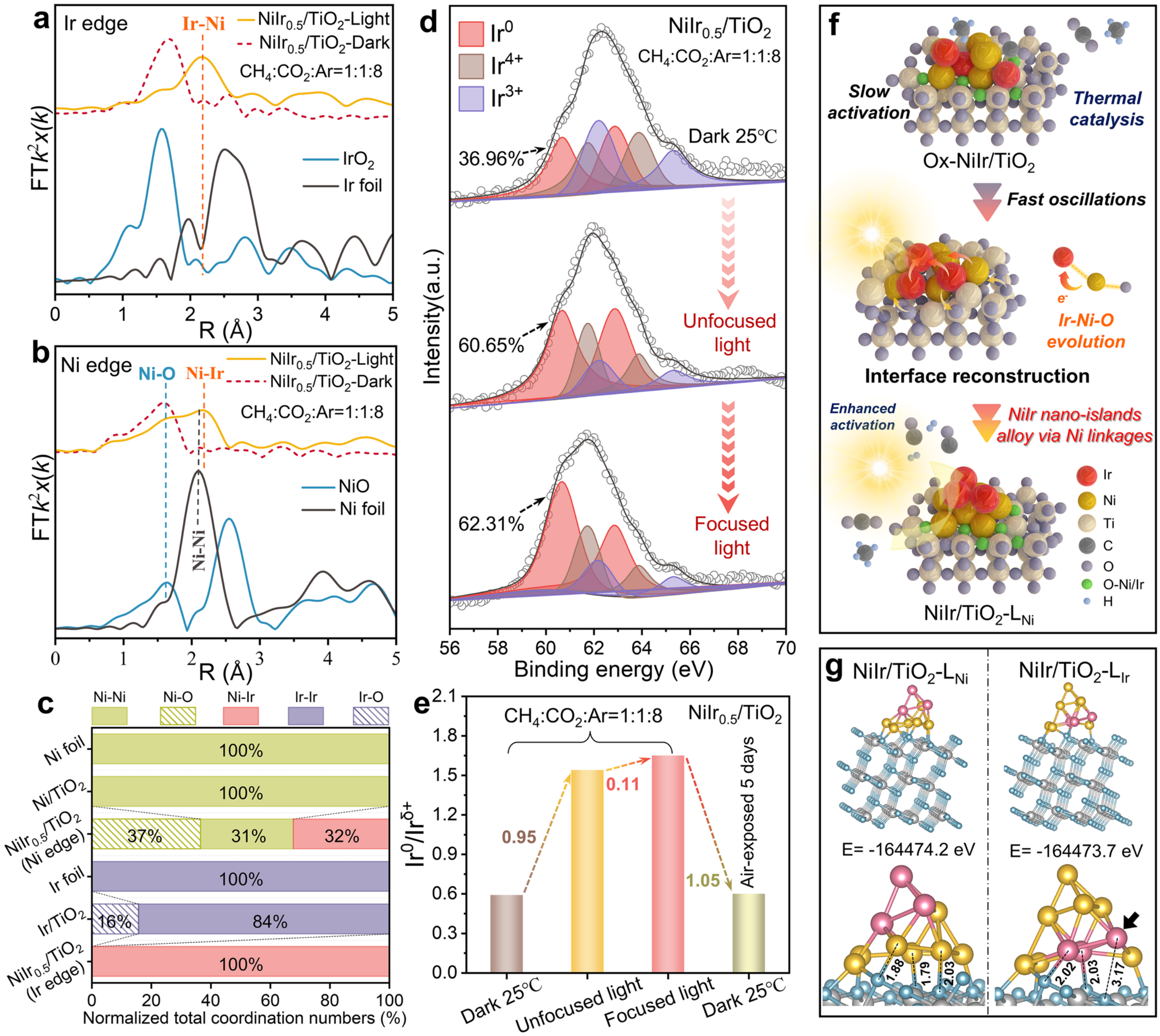

Fig. 3 | In situ XAS and NAP-XPS analysis of light-induced structural dynamics in NiIr/TiO$_2$. a, b In situ k^2-weighted Fourier transform of Ir L$_3$-edge **a** and Ni K-edge **b** EXAFS spectra for NiIr$_{0.5}$/TiO$_2$ during light-driven DRM conditions (CH$_4$: CO$_2$: Ar =1: 1: 8, 3.89 W cm^{-2}; data are not phase-corrected). **c** Normalized coordination numbers (CN) of different samples from EXAFS fitting. **d** In situ NAP-XPS spectra of Ir 4*f* for NiIr$_{0.5}$/TiO$_2$ under different irradiation conditions in a gas flow of CH$_4$: CO$_2$: Ar =1: 1: 8 (Unfocused light: 1.58 W cm^{-2}; focused light: 3.89 W cm^{-2}). **e** Ir^0/Ir$^{\delta+}$ ratio evolution of NiIr$_{0.5}$/TiO$_2$ during in situ NAP-XPS conditions and post-air exposure, derived from deconvolution of the XPS spectra. **f** Schematics of light induced oscillatory of NiIr/TiO$_2$-L$_{Ni}$ formation. **g** DFT-optimized structures of NiIr/TiO$_2$-L$_{Ni}$ and NiIr/TiO$_2$-L$_{Ir}$. The key distances between Ni/Ir linkages and TiO$_2$ are annotated in black font. Ir, Ni, Ti, and O atoms are shown in pink, yellow, grey, and blue colors.

weakening of metal-support bonds, a phenomenon known to induce structural dynamics under illumination[22,44,45]. To confirm that the improved catalytic activity is induced by light-driven structural reorganization, DRM reaction experiment with external heating (Supplementary Fig. 34 and Note 6) were conducted. Under light irradiation with additional heating, a gradual decline in activity is observed over 30 min after the light is turned off. This is attributed to the immediate loss of the photoelectric–photothermal synergy, while the structural reversion of the alloy occurs more slowly, underscoring that light-induced structural reorganization together with the photoelectric-photothermal effect jointly contribute to the high DRM performance of the NiIr$_{0.5}$/TiO$_2$ catalyst.

Intermediates tracking and photoexcited charge transfer investigation

In situ synchrotron radiation-diffuse reflectance infrared Fourier transform spectroscopy (SR-DRIFTS) analysis during CO$_2$-CH$_4$ co-adsorption revealed distinct molecular activation patterns on NiIr$_{0.5}$/TiO$_2$ under dark conditions (Fig. 4a and Supplementary Fig. 35a). Characteristic vibrational modes emerged at 3014/1304 cm^{-1} (CH$_4$ deformation), 2346 cm^{-1} (C = O stretching), 1354 cm^{-1} (OCO stretching vibration, ν(OCO)), and 1536 cm^{-1} (monodentate carbonate, m-CO$_3^{2-}$), confirming robust adsorption of both reactants on partially oxidized NiIr nanoclusters. Temperature-programmed desorption (TPD) (Fig. 4b, Supplementary Fig. 35b) further demonstrated that NiIr$_{0.5}$/TiO$_2$ exhibited high CH$_4$ chemisorption with a prominent desorption peak at 417 °C attributed to Ni-Ir dual sites, while maintaining stable CO$_2$ adsorption through ensemble-dependent Ni or Ir adsorption at 546 °C.

Light irradiation or external heating induced surface intermediates over NiIr/TiO$_2$-L$_{Ni}$ during DRM reaction as monitored by time-resolved SR-DRIFTS (Fig. 4c-f). Under focused light, the complete conversion of m-CO$_3^{2-}$ to intensified ν(OCO) indicates light-triggered formation of NiIr/TiO$_2$-L$_{Ni}$, optimizing CO$_2$ adsorption configuration

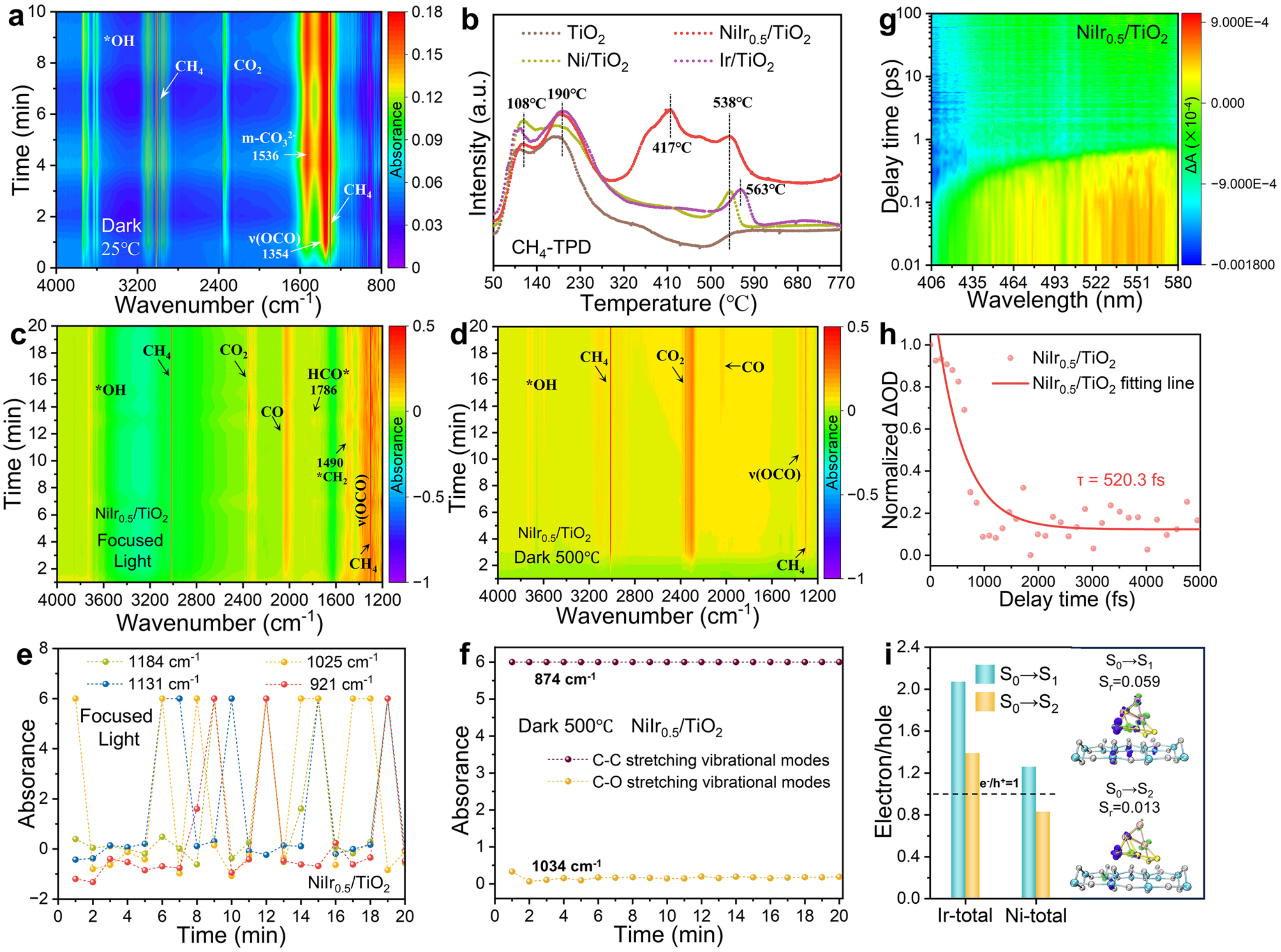

Fig. 4 | Time-resolved in situ tracking of reaction intermediates and photo-excited charge dynamics in NiIr/TiO$_2$. a In-situ SR-DRIFTS of NiIr$_{0.5}$/TiO$_2$ during CO$_2$-CH$_4$ co-adsorption in the dark (25 °C, CH$_4$: CO$_2$: Ar =1: 1: 8). **b** CH$_4$-TPD profiles of TiO$_2$, Ni/TiO$_2$, NiIr$_{0.5}$/TiO$_2$, and Ir/TiO$_2$. **c, d** In-situ SR-DRIFTS (4000–1200 cm^{-1}) of NiIr$_{0.5}$/TiO$_2$ under 3.89 W cm^{-2} focused light (**c**) vs. 500 °C dark heating (**d**) in a gas flow of CH$_4$: CO$_2$: Ar =1: 1: 8. **e, f** Time-resolved evolution of dominant sub-1200 cm^{-1} SR-DRIFTS peaks under focused light **e** and dark heating **f**. **g** 2D fs-TA spectroscopy mapping of NiIr$_{0.5}$/TiO$_2$. **h** Normalized fs-TA decay kinetics of NiIr$_{0.5}$/TiO$_2$ at 560 nm. **i** TD-DFT calculated electron-hole pairs distribution on NiIr/TiO$_2$-L$_{Ni}$ under S$_0$→S$_1$/S$_2$ excitations, and the corresponding electron/hole (e$^-$/h$^+$) ratio statistics of total Ir and Ni sites. The green and purple group represent the distribution of electrons and holes, respectively. The isosurface level is 0.005 e Å^{-3}. Ir, Ni, Ti, and O atoms are shown in pink, yellow, grey, and blue colors, respectively.

on NiIr alloy sites. Continuously detected gaseous CO (2024 cm^{-1}), characteristic vibrations of HCO* (1786 cm^{-1}) and *CH$_2$ (1490 cm^{-1})[8,46], confirmed efficient light-driven DRM activity (Fig. 4c). In contrast, dark thermal activation at 500 °C resulted in gradual emergence of attenuated CO signals after 12 min (Fig. 4d), aligning with its poor catalytic performance. Notably, transient intermediate signatures between 1120-920 cm^{-1} (Fig. 4e, Supplementary Fig. 36a) demonstrated ultrafast generation and decomposition of CH$_x$O* species[37,47] under illumination. Conversely, thermal catalysis produced prominent C-C stretching vibrations (974 cm^{-1})[48] (Fig. 4f, Supplementary Fig. 36b), consistent with coke accumulation observed in Supplementary Fig. 16. Isotopic mass spectrometry (Supplementary Fig. 37) revealed that photo-activated *O species primarily originated from CO$_2$ dissociation; these *O species combined with *CH$_x$ fragments to form metastable CH$_x$O* intermediates, establishing a dehydrogenation-dominated pathway that suppressed carbon deposition. Comparative studies of monometallic systems (Supplementary Fig. 38) highlighted the necessity of Ni-Ir synergy. Ni/TiO$_2$ exhibited negligible CO production with C-C coupling signals (873/893 cm^{-1}), while Ir/TiO$_2$ promoted *COOH formation (1678 cm^{-1}) via RWGS pathways. These findings underscore the necessity of Ni-Ir interaction in maintaining both C-H activation kinetics and intermediate stabilization.

To dissect photogenerated charge dynamics, femtosecond transient absorption (fs-TA) spectroscopy was employed (Fig. 4g, Supplementary Fig. 39a-c). Upon 325 nm excitation, all samples exhibited a ground-state bleach (GSB) at ca. 415 nm, reflecting the excited state relaxation[49]. Accompanied by excited state absorption (SA) between 460–570 nm, arising from electronic transitions from the singlet state (S$_1$) to higher energy excited states (S$_n$)[50]. Notably, NiIr$_{0.5}$/TiO$_2$ displayed the pronounced TA intensity, confirming NiIr alloy-enhanced charge separation. Time-decay fitting of the SA signal at 560 nm (Fig. 4h and Supplementary Fig. 39d-f) revealed a 520.3 fs lifetime for NiIr$_{0.5}$/TiO$_2$, which was markedly longer than TiO$_2$ (110.9 fs) or Ni/TiO$_2$ (233.1 fs), directly evidencing retarded charge recombination via Ni-Ir interaction. In addition, compared to pure TiO$_2$, NiIr nanoclusters show enhanced photocurrent density, lower electrochemical impedance, and quenched PL intensity; these respectively indicate stronger charge separation, faster charge transfer, and a greater number of effective photocarriers collected for reactions (Supplementary Fig. 39g-i and Note 7).

Ground-state and excited-state calculations resolved the interfacial charge transfer mechanism. Electron-density distributions (Supplementary Fig. 40a-d and Note 8) indicate Ni-mediated charge polarization enriches electrons at Ir sites. Simultaneously, density-of-states profiles (Supplementary Fig. 40e-h) reveal that NiIr alloy-induced d-band center modulation optimizes the trade-off between adsorption strength and intermediate desorption kinetics, suppressing both carbon deposition and parasitic reactions. Time-dependent DFT (TD-DFT) simulations (Fig. 4i) further identified excitation-dependent charge redistribution on NiIr/TiO_2-L_{Ni}. Electrons in photoexcited states preferentially accumulate at Ir sites distal to the TiO_2 interface, designating these Ir atoms as primary active centers for CO_2 reduction or H-H coupling during DRM. Electron/hole (e^-/h^+) ratio statistics reveal preferential electron capture at both Ir and Ni sites under the $S_0 \rightarrow S_1$ excited state, evidencing electron migration from the TiO_2 support to NiIr nanoclusters. The $S_0 \rightarrow S_2$ excited state exhibits a smaller *S*r index (the geometric mean overlap function of hole and electron distributions), representing less overlap between the electron and hole, and further indicating superior charge separation. Mechanistically, $S_0 \rightarrow S_2$ promotes hole accumulation at Ni sites alongside electron enrichment at Ir sites, which creates a spatial charge segregation that drives photoexcited electrons toward Ir centers in higher-energy states. Computational analysis of chemical bond strength changes between the ground and excited states (Supplementary Table 6) provides further mechanistic insight. The photoinduced charge transfer weakens the chemical bonds, which synergizes with thermal effects, facilitates atomic rearrangement into a more stable configuration. A detailed comparison reveals a more pronounced bond energy difference between the excited state and the ground state in Ir-O bond (-28.06 kJ mol^{-1}) compared to that of the Ni-O bond (-9.36 kJ mol^{-1}). This indicates a preferential destabilization and breaking of the Ir-O bonds, thereby facilitating the migration of Ir atoms. Furthermore, under the excited state, the Ni-Ir bond (92.35 kJ mol^{-1}) is stronger than the Ir-O bond (69.64 kJ mol^{-1}). These bond energy differences provide support for the formation of the Ni-Ir alloy under light irradiation.

Synergy between Ni-mediated charge transfer and Ir-tailored adsorption establishes a self-optimizing catalytic cycle under illumination. Transient intermediate tracking demonstrates light-driven suppression of coking pathways through metastable CH_xO^* formation, while fs-TA reveals hierarchical charge transfer from $TiO_2 \rightarrow Ni \rightarrow Ir$. This dual functionality, achieved through NiIr nano-island architecture, enables simultaneous enhancement of photogenerated carrier utilization and surface reaction kinetics.

Theoretical calculation of reaction mechanism and natural sunlight validation

DFT calculations (Supplementary data 1) coupled with in situ spectroscopic evidence unraveled the light-induced dynamic restructuring mechanism governing reaction pathway selectivity. Site-resolved adsorption analysis on the NiIr/TiO_2-L_{Ni} model (Supplementary Fig. 41) revealed that the Ir^1-Ni^3 asymmetric sites exhibited optimal CO_2 adsorption (E_{ads} = -1.22 eV) via ν(OCO) configuration. In contrast, the Ni^1-Ni^2-O domain exhibited negligible CO_2 adsorption in the form of m-CO_3^{2-} (E_{ads} = −0.03 eV). Charge complementarity between $Ni^{\delta+}$ and $Ir^{\delta-}$ drives complete CO_2 adsorption mode transition from m-CO_3^{2-} under dark to ν(OCO) upon illumination, as evidenced by time-resolved SR-DRIFTS. CH_4 preferentially anchors at Ir^2 sites through H···Ir interaction, where accumulated electrons from Ni-mediated interfacial transfer stabilize the C-H scission transition state. Comparative studies confirmed NiIr/TiO_2-L_{Ni}'s superior adsorption (Supplementary Fig. 42), with Ni/TiO_2 performing poorest, which is consistent with TPD trends.

For the initial bond cleavage of CO_2 and CH_4 molecules as shown in Fig. 5a-b and Supplementary Figs. 43–44, NiIr/TiO_2-L_{Ni} demonstrates both thermodynamic and kinetic advantages. Compared to monometallic Ni/TiO_2 and Ir/TiO_2, NiIr/TiO_2-L_{Ni} exhibits a significantly greater energy reduction after direct C = O scission of CO_2 and the first C-H scission of CH_4, indicating its superior thermodynamic favorability. Meanwhile, NiIr/TiO_2-L_{Ni} exhibits activation energies (Ea) of the transition states at +0.26 eV for C = O scission and +0.30 eV for C-H scission. These values are lower than the transition state barriers for the first C-H scission of CH_4 and direct CO_2 scission on Ni/TiO_2 and Ir/TiO_2, indicating the kinetic advantage of the nanoisland NiIr alloy. Supplementary Fig. 45 further compares the pathway of direct C = O scission of CO_2 with the indirect activation route via *COOH pathways. The results reveal Ir/TiO_2's propensity for *COOH formation, aligning with in situ SR-DRIFTS detected RWGS activity and a suboptimal H_2/CO ratio. In contrast, NiIr/TiO_2-L_{Ni} enables concerted C = O scission, where Ni site stabilizes dissociative oxygen and Ir site coordinates carbon, directly yielding CO and *O species.

Regarding the subsequent activation process after the initial bond cleavage of CH_4, *CH_3 may undergo further direct C-H scission until a C atom remains. Alternatively, *CH_3 can be assisted by activation through combination with O species from CO_2 activation (O_{CO2}) or lattice oxygen (O_L). Figure 5c compares the thermodynamic energy changes before and after the reaction for these three possible activation pathways. The results show that the sequential direct C-H scission pathway (*$CH_3 \rightarrow$ *$CH_2 \rightarrow$ *CH → *C) on NiIr/TiO_2-L_{Ni} requires prohibitively high energy, particularly 1.18 eV for cleaving the second C-H bond. For the *O-assisted C-H scission routes, O_L-assisted pathways proved unfavorable due to the high *CH_3 migration energy of 1.30 eV. Conversely, *O species from CO_2 dissociation adsorbed on Ni sites in NiIr/TiO_2-L_{Ni} enabled thermodynamically favorable *CH_3O formation with ΔE = -0.61 eV, and subsequent dehydrogenation required only 0.29 eV, consistent with isotopic labeling results. Comparative studies between NiIr/TiO_2-L_{Ni} and monometallic Ni/TiO_2 and Ir/TiO_2 in Supplementary Fig. 46 further highlight the optimal performance of NiIr/TiO_2-L_{Ni}. Specifically, in *O_{CO2}-assisted pathways, while Ni/TiO_2 struggled with CH_4 activation exhibiting a second C-H barrier of 0.75 eV and Ir/TiO_2 suffered from poor *O stabilization, the NiIr alloy achieved balanced kinetics through asymmetric Ni-Ir sites. Figure 5d quantitatively contrasts key steps that Ir/TiO_2 excels in initial C-H scission but falters in *CH_3O stabilization, whereas NiIr/TiO_2-L_{Ni} synergizes Ir's C-H activation prowess with Ni's oxygen affinity, enabling stepwise dehydrogenation without carbon buildup. Product desorption studies (Supplementary Fig. 47) revealed moderate H_2/CO adsorption on NiIr/TiO_2-L_{Ni}, ensuring sustained catalytic turnover. In addition, O_x-NiIr/TiO_2 exhibited excessive CO_2 adsorption but poor C = O scission capacity (Supplementary Fig. 48), while thermal conditions promoted direct CH_4 cracking into carbon deposits (Supplementary Fig. 49). This starkly contrasts with photoinduced NiIr nano-island alloy, underscoring light's critical role in structural optimization. We note that our DFT calculations are based on idealized slab models and static configurations and therefore provide qualitative insight into trends rather than a complete description of the real catalyst under operando conditions.

We also conducted an outdoor DRM experiment under actual sunlight using a Fresnel lens for light concentration (Fig. 5e-f). During 2-hour sunlight irradiation, light intensity varied from 3.22 to 4.08 W cm^{-2}, catalyst temperature ranged 438–505 °C. $NiIr_{0.5}/TiO_2$ exhibits a maximum syngas generation rate of 2782 mmol g_{cat}^{-1} h^{-1} (65.7% CO_2 conversion) with 20% feed gas flow, indicating the feasibility of this system in the utilization of sunlight. Figure 5f and the Supplementary Movie 1 show the real-time colorimetric response of the $PdCl_2$ indicator during the DRM reaction under focused natural sunlight. After illumination, the originally yellow $PdCl_2$ solution gradually turns black, indicating that a large amount of CO generated in the system adsorbs on the Pd^{2+} sites and reduces them to Pd^0, verifying the high efficiency of the NiIr/TiO_2 system under natural sunlight.

Figure 5g illustrates the overall reaction mechanism. Under light excitation, O_x-NiIr/TiO_2 undergoes interfacial charge oscillations, with

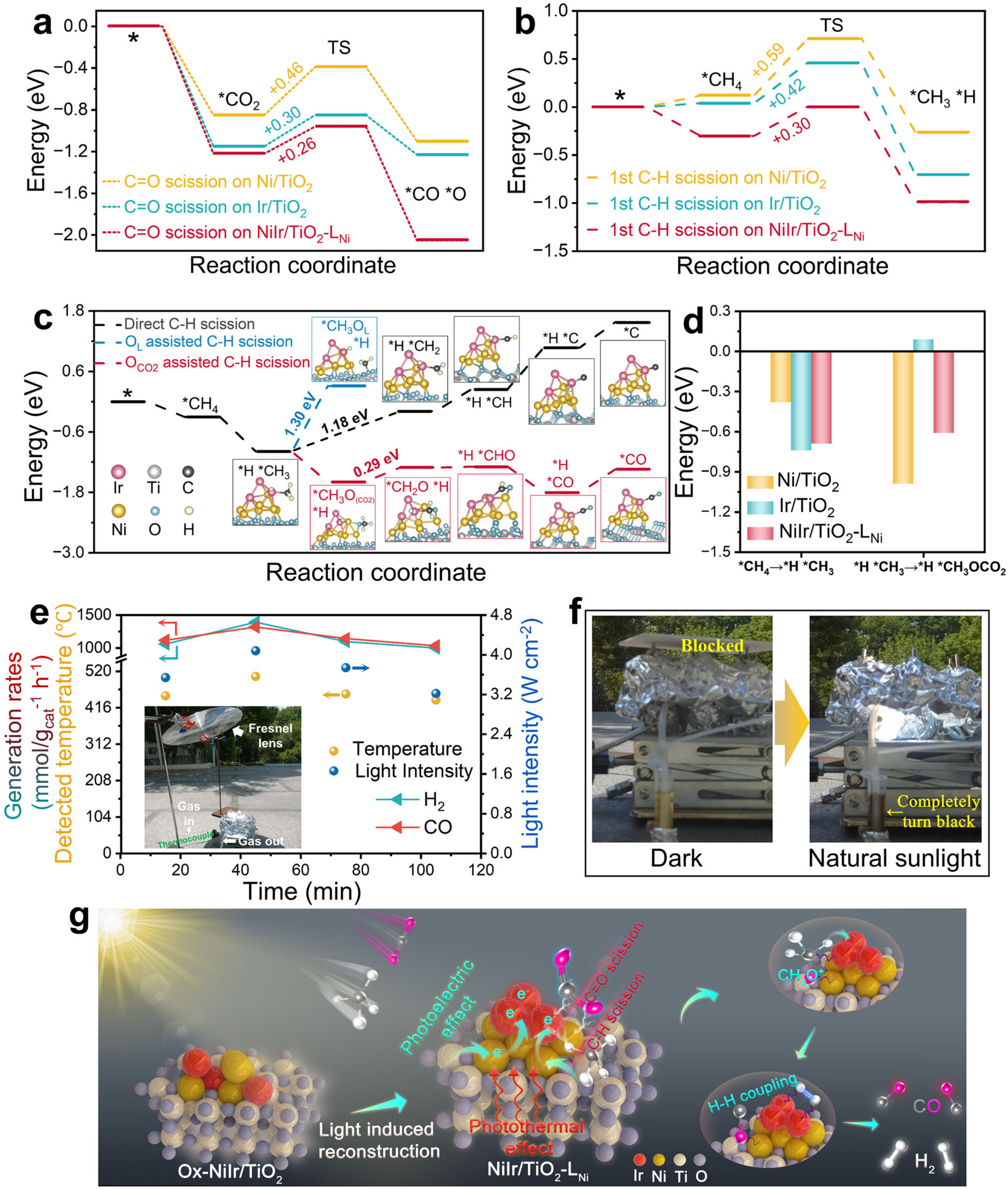

Fig. 5 | DFT calculations of reaction pathway and natural sunlight experiments. **a** Reaction energy profiles (including transition states) for C = O bond scission of CO_2 on NiIr/TiO_2-L_{Ni}, Ni/TiO_2, and Ir/TiO_2 models. **b** Reaction energy profiles (including transition states) for C-H bond scission of CH_4 on NiIr/TiO_2-L_{Ni}, Ni/TiO_2, and Ir/TiO_2 models. **c** Reaction energy profiles for different CH_4 activation pathways on NiIr/TiO_2-L_{Ni} model. **d** Energy evolution of key steps (pink-shaded indicator in Supplementary Fig. 46a) during the first C-H scission of CH_4 and the formation of *CH_3O intermediate. Ir, Ni, Ti, and O atoms are shown in pink, yellow, grey, and blue colors, respectively. **e** DRM performance over $NiIr_{0.5}$/TiO_2 under concentrated natural sunlight, with measured reaction temperature and incident light intensity (CH_4: CO_2: Ar =1: 1: 8, 20 ml min^{-1}). Inset: experimental setup. **f** DRM reaction demonstration under concentrated sunlight, with gas outlet directly interfaced to a $PdCl_2$ indicator solution for CO detection. **g** Schematic illustration of light-driven DRM mechanism.

electrons sequentially transferring from the TiO_2 to Ni sites and subsequently to Ir atoms. This triggers the upward migration of Ir atoms, leading to the formation of NiIr nano-island alloys. A portion of Ni atoms act as linkages, spatially isolating the NiIr alloy from the support to form the NiIr/TiO_2-L_{Ni} configuration. During light-driven DRM reaction, photoelectric effects dominate the activation of C-H and C = O bonds at NiIr alloy sites, coupled with efficient H-H coupling via localized photogenerated electrons. Concurrently, the oxygen affinity of the Ni linkages steers the reaction pathway toward the formation of key CH_xO^* intermediates, thereby achieving robust coking resistance. Meanwhile, photothermal effects facilitate molecular vibrations, intermediate migration, and product desorption. The synergistic interplay of photoelectric and photothermal effects on the NiIr nano-island alloy enables highly efficient and stable DRM performance.

In summary, this work reveals that light-induced NiIr nano-island alloy formation enables efficient DRM by synergizing photoelectric and photothermal effects. The interfacial charge oscillation mechanism not only stabilizes ultrafine alloy architectures against sintering but also creates dual-active sites. Specifically, Ni linkages with oxygen affinity favor coke suppression, while Ir sites modulated by Ni optimize reactant activation. Our experimental method for decoupling photoelectric/photothermal contributions reveals that localized electron transfer dominates bond cleavage selectivity, whereas thermal effects primarily govern mass transport. The achieved 25.0% LTFE and 100-h stability under practical feed conditions underscore the viability of solar-driven DRM. Importantly, the methodology combining in situ structural analysis with charge dynamics kinetics provides a universal approach to probe light–matter interactions in heterogeneous catalysis.

Methods

Catalyst preparation

O_x-NiIr/TiO_2 catalysts were synthesized via an optimized directional adsorption strategy[23]. Typically, 200 mg of ground TiO_2 nanosheets was dispersed in 0.01 M NaOH aqueous solution. After 3 h, the TiO_2 was centrifuged and redispersed in deionized (DI) water through multiple cycles until the supernatant reached pH=9, ensuring a negatively charged TiO_2 surface for cation adsorption. $NiCl_2$ (Sigma-Aldrich) aqueous solution (containing Ni equivalent to 1 wt% of TiO_2) was added to the TiO_2 suspension and stirred for 12 h prior to centrifugation. Complete metal cation adsorption was confirmed by testing the first supernatant with $NaBH_4$ (Thermo Fisher), which showed no color change. The cation-loaded TiO_2 was washed with DI water and dried at 60 °C for 12 h. Co^{2+} ($Co(NO_3)_2{\cdot}6H_2O$, Macklin), Fe^{3+}($FeCl_2{\cdot}6H_2O$, Aladdin), and $Pt(NH_3)_4^{2+}$ ($[Pt(NH_3)_4]Cl_2$, Sigma-Aldrich) cations were similarly adsorbed using their respective chloride salts.

The dried cation-loaded TiO_2 was subsequently used for complex metal anion adsorption $IrCl_6^{3-}$(Na_3IrCl_6, Sigma-Aldrich), $PtCl_4^{2-}$ (K_2PtCl_4, Sigma-Aldrich), $PdCl_4^{2-}$ (Na_2PdCl_4, Sigma-Aldrich), $AuCl_4^-$ ($HAuCl_4{\cdot}3H_2O$, Sigma-Aldrich), and $RuCl_6^{2-}$$(NH_4)_2RuCl_6$, Sigma-Aldrich) with controlled theoretical anion/cation atomic ratios. Anion solutions were prepared via a phase-transfer method using tetrabutylammonium cations (TBA^+) in dichloromethane (TBA^+/anion molar ratio = 3) under vortex mixing. After centrifugation, the dichloromethane phase was retained, and mixed with cation-loaded TiO_2 in dichloromethane. After 12 h of stirring, TiO_2-supported double complex salts were centrifuged, dried at room temperature, and reduced under 5% H_2 flow at 400 °C for 30 min. Monometallic TiO_2-supported catalysts (Ni^{2+} and Ir^{3+}) were prepared analogously without anion adsorption steps.

Catalytic reactivity measurements

Light-driven DRM experiments were performed in a custom quartz reactor (Supplementary Fig. 9) at 0.1 MPa without extra heating. The reactor features an outer layer for condensate circulation and an inner chamber containing a quartz sand bed for supporting catalyst and optimize gas distribution. A type-K thermocouple (0–1150 °C range, 0.5 mm diameter, ±0.1 °C accuracy) was embedded in the quartz sand bed, with a 90°-bent tip protruding 1.0 mm above the surface. The thermocouple was pre-calibrated against standard reference sources, and its performance was verified at multiple temperature setpoints to ensure consistency across the experimental range. T_{Center} (the center temperature of catalyst surface) was detected by the thermocouple probe placed in direct contact with the upper surface of the catalyst at its center, enabling capture of the highest local temperature under irradiation (as shown by the red indicator line representing the thermocouple in Supplementary Fig. 9). This arrangement minimizes the thermal resistance effect by avoiding indirect measurement through the gas phase or reactor materials. Infrared (IR) thermography was used to validate the accuracy of T_{Center} measurements from the thermocouple probe. T_{AVG} (average surface temperature) was obtained by moving the thermocouple probe, measuring temperatures at five different points on the catalyst surface (center and edges) and using the formula below:

$$T_{\mathrm{AVG}} = \frac{\bar{T}_{\mathrm{Center}}}{3} + \frac{2\times\bar{T}_{\mathrm{Edge}}}{3} \tag{1}$$

Catalyst (5 mg) was dispersed in DI water (1.0 mL), spread on a quartz fiber membrane, and vacuum-dried. The membrane was positioned on the quartz sand bed, and depressed by a tweezer align the thermocouple tip flush with the catalyst surface. Real-time temperature monitoring at catalyst center and edge positions was achieved by adjusting the thermocouple position via its stretchable connector. Note that unlike conventional temperature probes positioned below the catalyst, our small-diameter temperature probes are placed directly on the catalyst surface, enabling more accurate and sensitive temperature measurement. Prior to irradiation using a 300 W Xe lamp (PLS-SXE 300 +, Beijing PERFECTLIGHT; spectral range: 300–1000 nm), the reactor was introduced with CH_4: CO_2 (1:1) gas mixture at 20 mL min^{-1}. A biconvex lens (diameter: 70 mm) was employed for light focusing. Light intensity was controlled by adjusting lamp current and measured using an optical power meter (range: 0–20 W, resolution: 1 mW).

Thermal catalytic tests were conducted in a dedicated reactor (PLR-PTSR II, Beijing PERFECTLIGHT) under dark conditions, using identical catalyst supporting and thermocouple configurations to those in the custom quartz reactor. Natural sunlight experiments utilized the custom quartz reactor with Fresnel lens focusing. All other experimental parameters (gas flow, catalyst weight, etc.) remained consistent across light-driven, thermal, and natural sunlight conditions.

The monochromatic light activity tests were carried out in a dedicated reactor (PLR-PTSR II, Beijing PERFECTLIGHT) with external heating at 500 °C. A 300 W Xenon lamp was used as the light source, coupled with optical filters to obtain monochromatic light of specific wavelengths. In each test, an optical power meter was used to accurately measure and calibrate the incident light intensity in front of the reactor window. Dividing the measured syngas generation rates by the light intensity under the corresponding monochromatic light yields the contributions of monochromatic light at different wavelength bands to the activity per unit light intensity. All other test conditions were consistent with those of the light-driven conditions.

The CO products were analyzed by GC with a flame-ionization detector (FID). H_2 was analyzed by GC with a high-sensitivity thermal conductivity detector (TCD). The H_2 and CO generation rates were defined as follows:

$$R_{H_2} = C_{H_2}^{out} \times F_{out} \times 60/(V_m \times M) \quad (2)$$

$$R_{CO} = C_{CO}^{out} \times F_{out} \times 60/(V_m \times M) \quad (3)$$

Where R_{H_2} (mmol g_{cat}^{-1} h^{-1}) and R_{CO} (mmol g_{cat}^{-1} h^{-1}) are the H_2 and CO generation rates, respectively. The $C_{H_2}^{out}$ (dimensionless) and C_{CO}^{out} (dimensionless) are the concentrations of H_2 and CO detected by gas chromatography. F_{out} (ml/min) is the space velocity of the gas exiting the reactor, V_m (L/mol) is the gas molar volume under standard conditions, and M (g) is the mass of catalyst. 60 refers to the exponent needed to convert ml/min into the standard unit ml/h.

The CH_4 and CO_2 conversions were defined as follows:

$$CH_4\text{conversion} : X_{CH_4}(\%) = (C_{CH_4}^{in} - C_{CH_4}^{out})/C_{CH_4}^{in} \times 100 \quad (4)$$

$$CO_2\textit{conversion} : X_{CO_2}(\%) = (C_{CO_2}^{in} - C_{CO_2}^{out})/C_{CO_2}^{in} \times 100 \quad (5)$$

Where $C_{CH_4}^{in}$ (dimensionless) and $C_{CH_4}^{out}$ (dimensionless) indicate the inlet and outlet concentration of products detected by gas chromatography, respectively.

Total carbon balance is considered using the following equation:

$$\text{Total carbon balance} = \frac{C_{CO}^{out} + C_{CO_2}^{out} + C_{CH_4}^{out}}{C_{CO_2}^{in} + C_{CH_4}^{in}} \times 100 \quad (6)$$

TOF under kinetics-controlled regime per second can be calculated with the following equation:

$$\text{TOF}(S^{-1}) = \frac{0.5 \times N_{\text{NumberofproducedH}_2\text{persecond}} + 0.5 \times N_{\text{NumberofproducedCOpersecond}}}{N_{\text{activemetal}} \times \text{Dispersion}} \quad (7)$$

The LTFE (η) was determined with the following equation:

$$\eta = \frac{(R_{H_2} \times \triangle_C H_{H_2}^{o} + R_{CO} \times \triangle_C H_{CO}^{o} + R_{CH_4} \times \triangle_C H_{CH_4}^{o}) \times M}{P_{irradiation}} \quad (8)$$

Where R_{H_2} (mmol g_{cat}^{-1} h^{-1}), R_{CO} (mmol g_{cat}^{-1} h^{-1}) and R_{CH_4} (mmol g_{cat}^{-1} h^{-1}) are the H_2 generation rates, CO generation rates, and CH_4 conversion rates. $\triangle_C H_{H_2}^{o}$, $\triangle_C H_{CO}^{o}$, and $\triangle_C H_{CH_4}^{o}$ are the standard combustion heats (298.15 K) of H_2, CO, and CH_4 as fuels, respectively. Note that the $\triangle_C H_{CO_2}^{o}$ is 0. M (g) is the mass of catalyst. $P_{irradiation}$ (W) is the irradiation power.

Characterization

HAADF-STEM imaging was performed on an aberration-corrected FEI Themis Z instrument, with a convergence semi-angle set to 11 mrad and annular detection ranges of 59 mrad (inner) and 200 mrad (outer). Elemental mapping and EDS analysis were carried out utilizing the integrated four-quadrant Super-X detector system. Powder XRD measurements were obtained using a Rigaku D/MAX 2550 diffractometer equipped with Cu Kα radiation (λ = 1.5406 Å), operating at 40 kV and 40 mA, with 2θ scanned from 10° to 80°. Raman spectroscopy was performed on a Renishaw in Via system using a 532 nm laser excitation source. UV−Vis-NIR diffuse reflectance spectra were recorded using a Varian Cary 500 spectrophotometer equipped with an integrating sphere, using $BaSO_4$ as a reference. For sample preparation, the powder sample was pressed into a flat, uniform pellet in a culture dish to ensure data reliability and reproducibility. The absorbance was represented by the Kubelka-Munk function:

$$F(R)(\text{where } F(R) = (1 - R)^2/2R) \quad (9)$$

which is derived from the measured reflectance data. Inductively coupled plasma atomic emission spectrometry (ICP-AES, Varian 730-ES, Agilent) quantified the metal loadings of catalysts. Thermogravimetric analysis (TGA) of spent catalysts was conducted on a Netzsch STA 449 F5 analyzer under air flow (50 mL min^{-1}), heating from 100 °C to 800 °C at 10 °C•min^{-1}. Temperature-programmed desorption (TPD) experiments were performed on an Auto Chem II 2920 (Micromeritics, USA) in pure He, ramping to 770 °C at 10 °C•min^{-1}. H_2-O_2 titration was performed on a temperature programmed chemisorption analyzer (VDSorb-91i) to measure metal dispersion. Photoluminescence (PL) spectra were acquired at room temperature using a Cary Eclipse fluorescence spectrometer (Agilent). Femtosecond transient absorption (fs-TA) spectroscopy was performed on a Helios pump-probe system (Ultrafast Systems, USA) with an 800 nm Ti:sapphire laser (Coherent Legend, 85 fs pulse width, 1 kHz repetition rate). The pump beam (325 nm, 80 μW) was generated via frequency doubling in a β-barium borate (BBO) crystal, while the probe beam (near-infrared continuum) monitored photoexcited states. Isotope labeling experiments employed a high-precision gas isotope mass spectrometer (Nu Instruments Horizon, UK): a 1:1 mixture of CH_4 and $C^{18}O_2$ was introduced into a batch reactor in the dark, followed by 15-min irradiation (300 W Xe lamp, 3.89 W cm^{-2}). Reaction products were cryogenically separated and analyzed for $C^{16}O$ and $C^{18}O$ isotopes.

In situ XAS measurements conditions

In situ XAS measurements at Ir L_3-edge and Ni K-edge were performed with Si (111) crystal monochromators at the BL14W Beam line at the Shanghai Synchrotron Radiation Facility (SSRF) (Shanghai, China). Typically, the powdered sample was pressed into a self-supporting wafer and placed into a reaction microdevice equipped with an extra window for light irradiation. Before the test, the sample surface was purged with Ar gas flow (50 ml min^{-1}). Afterwards, the gas mixture (CH_4: CO_2: Ar=1: 1: 8) or pure Ar was continuously introduced into the reactor with a flow rate of 20 mL min^{-1}. The microdevice was irradiated by the 300 W Xe lamp at the light intensity of 3.89 W cm^{-2}. The XAFS spectra were recorded in situ in the dark or after 10-min light irradiation using a Bruker 5040 4-channel Silicon Drift Detector (SDD) in fluorescence mode. All spectra were collected in ambient conditions. The data reduction and analysis of the XAFS spectra were conducted using the Demeter software package (ATHENA and ARTEMIS, respectively)[51]. All fits were performed in the R space with a k-weight of 2.

In situ NAP-XPS conditions

In situ NAP-XPS experiments were conducted on a SPECS Proven-X NAP instrument (Germany) equipped with a monochromatic X-ray source μ-FOCUS 600 NAP. Prior to the test, the sample surface was cleaned using an Ar gas flow (50 ml min^{-1}). Subsequently, a gas mixture (CH_4:CO_2:Ar=1:1:8) or pure Ar was continuously introduced into the reactor with a flow rate of 20 mL min^{-1}. The NAP-XPS spectra were recorded in situ in the dark or after 10-min light irradiation. The irradiation started with unfocused light at an intensity of 1.58 W cm^{-2} and then switched to focused light at 3.89 W cm^{-2}. Noted that under light conditions, no additional heating was applied, while under thermal conditions, the heating temperature was set at 500 °C. The NAP - XPS spectra were obtained with charge correction, using the C 1*s* binding energy of 284.60 eV as the energy reference.

In situ SR-DRIFTS conditions

In situ synchrotron radiation DRIFTS were performed at the BL01B Beam line at the Shanghai Synchrotron Radiation Facility (SSRF)

(Shanghai, China). The spectra were recorded by a Bruker infrared spectrometer (70 V) equipped with a liquid nitrogen-cooled mercury-cadmium-telluride (MCT) detector. Integrated with a high-brightness synchrotron radiation source, the setup achieved a spatial resolution near the theoretical diffraction limit, producing infrared spectra with high intensity and signal-to-noise ratio. The catalysts were first sealed in the chamber and purged with an Ar gas flow (50 ml min^{-1}). Subsequently, a flowed mixture gas (CH_4: CO_2: Ar=1: 1: 8) or pure Ar was introduced into the chamber with a flow rate of 20 mL min^{-1}. The chamber was then irradiated with the 300 W Xe lamp at a light intensity of 3.89 W cm^{-2}.

In situ CO-probe DRIFTS conditions

In situ CO-probe DRIFTS was recorded by a Fourier-transform infrared spectrometer (Bruker VERTEX 80 v, Germany) equipped with a designed reaction cell. Catalysts were initially degassed at 100 °C for 1 h and then cooled to 25 °C under a flow of Ar (50 ml min^{-1}). Subsequently, catalysts were exposed to a mixture of 20% CO in Ar (30 ml min^{-1}) for 30 min at 25 °C, which proved sufficient to saturate the catalyst surface. After saturation, the CO flow was replaced with an Ar flow (30 ml min^{-1}), and CO DRIFTS spectra were collected at 25 °C for 25 min. Then, the temperature was sequentially increased to 100 °C, 200 °C, 300 °C, and 400 °C, with spectra recorded at each temperature for 10 min.

Electrochemical measurements

Electrochemical measurements were conducted at room temperature using a Zahner Zennium potentiostat (Zahner-elektrik GmbH, Germany) with a three-electrode configuration: a fluorine-doped tin oxide (FTO) working electrode, a graphite counter electrode and a saturated calomel reference electrode (SCE). For working electrode preparation, 5 mg of catalyst was dispersed in 0.5 mL ethanol, and 20 μL of the slurry was drop-cast onto FTO (1 cm^2 active area) and dried under ambient conditions. Transient photocurrent responses were measured in N_2-saturated 0.5 M Na_2SO_4 under 300 W Xe lamp irradiation. The pH of the 0.5 M Na_2SO_4 electrolyte was measured to be 6.8 ± 0.1 ($n = 3$). Electrochemical impedance spectroscopy (EIS) was performed in the frequency range from 100 kHz to 0.1 Hz using an N_2-saturated potassium ferricyanide mixed electrolyte (25 mM $K_3Fe(CN)_6$, 25 mM $K_4Fe(CN)_6$, and 0.1 M KCl), whose pH was 7.0 ± 0.1 ($n = 3$). All electrochemical measurements were performed without iR correction. All potentials were converted to the reversible hydrogen electrode (RHE) scale according to the formula below.

$$E_{RHE} = E_{SCE} + 0.241\mathrm{V} + 0.059 \times \mathrm{pH} \tag{10}$$

where 0.241 V is the standard potential of the saturated calomel electrode versus RHE at 25 °C.

Theoretical calculations

All density functional theory (DFT) calculations were performed using the Materials Studio software and the Vienna ab initio simulation package (VASP)[52–54]. The exchange-correlation interactions were treated within the generalized gradient approximation (GGA), employing the Perdew–Burke–Ernzerhof (PBE) functional[55,56]. The projector augmented-wave (PAW) method was used to describe core-valence electron interactions, with a plane-wave basis set and a kinetic energy cutoff set to 400 eV. The Gaussian smearing scheme with a width of 0.05 eV was applied for partial orbital occupancy. Convergence criteria were set to 10^{-5} eV for electronic self-consistent iterations and 0.05 eV/Å for ionic relaxation during geometry optimization. A vacuum layer of 15 Å was added perpendicular to the surface model to avoid periodic interactions. For surface calculations, the Brillouin zone was sampled using a 2 × 2 × 1 Monkhorst–Pack k-point mesh. The adsorption energy was calculated according to the following formula:

$$E_{ad} = E_{A-S} - (E_S + E_A) \tag{11}$$

where $E_{A\text{-}S}$ is the energy of the slab together with the adsorbate, E_A is the total energy of the free adsorbate and E_S is the total energy of the bare slab.

The d band center (ε_d) was calculated as follow formula:

$$\varepsilon_d = \int_{-\infty}^{+\infty} n_d(\varepsilon)\varepsilon d\varepsilon \Big/ \int_{-\infty}^{+\infty} n_d(\varepsilon) d\varepsilon \tag{12}$$

The transition states corresponding to elementary reaction steps were located using a sequential approach combining the nudged elastic band (NEB) and dimer methods[57]. First, the reaction pathway connecting the reactant and product states was sampled using the NEB method, which represents the path as a discrete set of structural images. From this set, the image possessing the highest energy, indicative of the most probable transition state configuration, was selected. This structure subsequently served as the initial guess for precise transition-state optimization using the dimer method.

Excitation-dependent charge redistribution calculations are performed with ORCA software[58]. The functional employed was PBE0, and the basis set used was def2-SVP. (This basis set is an all-electron basis set for the first four periods and a pseudopotential basis set starting from the fifth period, so no mixed basis set is required.) The electron-hole structures were calculated using Multiwfn[59], and the visualization data were obtained using the visual molecular dynamics VMD software[60]. The geometric mean overlap function of hole and electron distributions (S_r) was calculated as follows:

$$\mathrm{Sr}(r) = \sqrt{[\rho^{hole}(\mathrm{r})\rho^{ele}(\mathrm{r})]} \tag{13}$$

ρ^{hole} and ρ^{ele} represent the electron density of the hole and the excited electron at the spatial position r, respectively.

Data availability

All data generated in this study are provided in the main text, supplementary information, source data and supplementary data 1 file. Source data are provided with this paper.

References

1. Tavasoli, A. & Ozin, G. Green syngas by solar dry reforming. *Joule* **2**, 571–575 (2018).
2. Song, Y. et al. Dry reforming of methane by stable Ni-Mo nanocatalysts on single-crystalline MgO. *Science* **367**, 777–781 (2020).
3. Meng, X. et al. Direct methane conversion under mild condition by thermo-, electro-, or photocatalysis. *Chem* **5**, 2296–2325 (2019).
4. Aresta, M., Dibenedetto, A. & Angelini, A. Catalysis for the valorization of exhaust carbon: from CO_2 to chemicals, materials, and fuels. technological use of CO_2. *Chem. Rev.* **114**, 1709–1742 (2014).
5. Palmer, C. et al. Dry reforming of methane catalysed by molten metal alloys. *Nat. Catal.* **3**, 83–89 (2020).
6. Zhu, Q. et al. Enhanced CO_2 utilization in dry reforming of methane achieved through nickel-mediated hydrogen spillover in zeolite crystals. *Nat. Catal.* **5**, 1030–1037 (2022).
7. Zhou, L. et al. Light-driven methane dry reforming with single atomic site antenna-reactor plasmonic photocatalysts. *Nat. Energy* **5**, 61–70 (2020).
8. Xiong, H. et al. Highly efficient and selective light-driven dry reforming of methane by a carbon exchange mechanism. *J. Am. Chem. Soc.* **146**, 9465–9475 (2024).
9. Li, Q. et al. Suppressive strong metal-support interactions on ruthenium/TiO_2 promote light-driven photothermal CO_2 reduction with methane. *Angew. Chem. Int. Ed.* **62**, e202300129 (2023).

10. Pakhare, D. & Spivey, J. A review of dry (CO_2) reforming of methane over noble metal catalysts. *Chem. Soc. Rev.* **43**, 7813–7837 (2014).
11. Mattos, L. V., Jacobs, G., Davis, B. H. & Noronha, F. B. Production of hydrogen from ethanol: review of reaction mechanism and catalyst deactivation. *Chem. Rev.* **112**, 4094–4123 (2012).
12. Li, X. et al. Advances in heterogeneous single-cluster catalysis. *Nat. Rev. Chem.* **7**, 754–767 (2023).
13. He, C. et al. Regulating atomically-precise Pt sites for boosting light-driven dry reforming of methane. *Angew. Chem. Int. Ed.* **63**, e202412308 (2024).
14. Li, X. et al. Functional CeO_x nanoglues for robust atomically dispersed catalysts. *Nature* **611**, 284–288 (2022).
15. Zhou, T. et al. Ultrafine metal nanoparticles isolated on oxide nano-islands as exceptional sintering-resistant catalysts. *Nat. Mater*. (2025).
16. Gashnikova, D. et al. Highly active oxidation catalysts through confining Pd clusters on CeO_2 nano-islands. *Angew. Chem. Int. Ed.* **63**, e202408511 (2024).
17. Marimuthu, A., Zhang, J. & Linic, S. Tuning selectivity in propylene epoxidation by plasmon mediated photo-switching of Cu oxidation state. *Science* **339**, 1590–1593 (2013).
18. Lee, B.-H. et al. Reversible and cooperative photoactivation of single-atom Cu/TiO_2 photocatalysts. *Nat. Mater.* **18**, 620–626 (2019).
19. Luo, S. et al. Light-induced dynamic restructuring of Cu active sites on TiO_2 for low-temperature H_2 production from methanol and water. *J. Am. Chem. Soc.* **145**, 20530–20538 (2023).
20. Ren, C., Li, Q., Ling, C. & Wang, J. Mechanism-guided design of photocatalysts for CO_2 reduction toward multicarbon products. *J. Am. Chem. Soc.* **145**, 28276–28283 (2023).
21. Jiang, H. et al. Light-driven CO_2 methanation over Au-grafted $Ce_{0.95}Ru_{0.05}O_2$ solid-solution catalysts with activities approaching the thermodynamic limit. *Nat. Catal.* **6**, 519–530 (2023).
22. Li, J. et al. Activating lattice oxygen in perovskite ferrite for efficient and stable photothermal dry reforming of methane. *J. Am. Chem. Soc.* **147**, 14705–14714 (2025).
23. Ding, K. et al. A general synthesis approach for supported bimetallic nanoparticles via surface inorganometallic chemistry. *Science* **362**, 560–564 (2018).
24. Zou, S. et al. Manufacturing single-atom alloy catalysts for selective CO_2 hydrogenation via refinement of isolated-alloy-islands. *Angew. Chem. Int. Ed.* **64**, e202412835 (2025).
25. Zhou, J. et al. Interfacial compatibility critically controls Ru/TiO_2 metal-support interaction modes in CO_2 hydrogenation. *Nat. Commun.* **13**, 327 (2022).
26. Li, X. et al. Controlling CO_2 hydrogenation selectivity by metal-supported electron transfer. *Angew. Chem. Int. Ed.* **59**, 19983–19989 (2020).
27. Tan, S. et al. Plasmonic coupling at a metal/semiconductor interface. *Nat. Photonics* **11**, 806–812 (2017).
28. Han, J. W., Park, J. S., Choi, M. S. & Lee, H. Uncoupling the size and support effects of Ni catalysts for dry reforming of methane. *Appl. Catal. B Environ.* **203**, 625–632 (2017).
29. Li, X. et al. Dry reforming of methane over Ni/La_2O_3 nanorod catalysts with stabilized Ni nanoparticles. *Appl. Catal. B Environ.* **202**, 683–694 (2017).
30. Pan, F. et al. A novel photo-thermochemical approach for enhanced carbon dioxide reforming of methane. *ChemCatChem* **10**, 940–945 (2018).
31. Zhang, Q. et al. Novel photoactivation promoted light-driven CO_2 reduction by CH_4 on Ni/CeO_2 nanocomposite with high light-to-fuel efficiency and enhanced stability. *Appl. Catal. B Environ.* **239**, 555–564 (2018).
32. Akri, M. et al. Atomically dispersed nickel as coke-resistant active sites for methane dry reforming. *Nat. Commun.* **10**, 5181 (2019).
33. Gao, Y. et al. Light-driven efficient dry reforming of methane over Pt/La_2O_3 with long-term durability. *J. Mater. Chem. A* **10**, 16016–16028 (2022).
34. Kushida, M., Yamaguchi, A. & Miyauchi, M. Photocatalytic dry reforming of methane by rhodium supported monoclinic TiO_2-B nanobelts. *J. Energy Chem.* **71**, 562–571 (2022).
35. Wu, J. et al. Engineering the oxygen vacancies enables Ni single-atom catalyst for stable and efficient C-H activation. *Appl. Catal. B Environ.* **314**, 121516 (2022).
36. Yang, Y. et al. Light-induced redox looping of a rhodium/$CeWO_3$ photocatalyst for highly active and robust dry reforming of methane. *Angew. Chem. Int. Ed.* **61**, e202200567 (2022).
37. Rao, Z. et al. Light-reinforced key intermediate for anticoking to boost highly durable methane dry reforming over single atom Ni active sites on CeO_2. *J. Am. Chem. Soc.* **145**, 24625–24635 (2023).
38. Tang, Y. et al. Enhanced dry reforming of CO_2 and CH_4 on photothermal catalyst Ru/$SrTiO_3$. *Appl. Catal. B Environ.* **338**, 123054 (2023).
39. Yao, Y. et al. Highly efficient solar-driven dry reforming of methane on a Rh/$LaNiO_3$ Catalyst through a light-induced metal-to-metal charge transfer process. *Adv. Mater.* **35**, 2303654 (2023).
40. He, Z. et al. Engineering an Ni-TiO_x interface for highly active and durable solar-driven dry reforming of methane. *Chem Catal* **4**, 101040 (2024).
41. Wang, B. et al. Single atom iridium decorated nickel alloys supported on segregated MoO_2 for alkaline water electrolysis. *Adv. Mater.* **36**, 2305437 (2024).
42. Zhao, G. F. & Zeng, Z. Geometrical and electronic structures of Au_mAg_n ($2 \le M + N \le 8$). *J. Chem. Phys.* **125**, 014303 (2006).
43. Liu, L. & Corma, A. Bimetallic sites for catalysis: from binuclear metal sites to bimetallic nanoclusters and nanoparticles. *Chem. Rev.* **123**, 4855–4933 (2023).
44. Sun, G. et al. Full utilization of noble metals by atom abstraction for propane dehydrogenation. *Science*, eadw3053 (2025). https://doi.org/10.1126/science.adw3053.
45. Guo, C. et al. Light-driven metal exsolution-redissolution of high-entropy oxide enabling high-performance dry reforming of methane. *Adv. Mater.* **37**, 2500928 (2025).
46. Zhang, W. et al. High-performance photocatalytic nonoxidative conversion of methane to ethane and hydrogen by heteroatoms-engineered TiO_2. *Nat. Commun.* **13**, 2806 (2022).
47. Li, X. et al. Selective visible-light-driven photocatalytic CO_2 reduction to CH_4 mediated by atomically thin $CuIn_5S_8$ layers. *Nat. Energy* **4**, 690–699 (2019).
48. Jiang, W. et al. Pd-modified ZnO–Au enabling alkoxy intermediates formation and dehydrogenation for photocatalytic conversion of methane to ethylene. *J. Am. Chem. Soc.* **143**, 269–278 (2021).
49. Wolff, C. M. et al. All-in-one visible-light-driven water splitting by combining nanoparticulate and molecular co-catalysts on CdS nanorods. *Nat. Energy* **3**, 862–869 (2018).
50. Wang, A. et al. Enhanced and synergistic catalytic activation by photoexcitation driven S–scheme heterojunction hydrogel interface electric field. *Nat. Commun.* **14**, 6733 (2023).
51. Ravel, B. & Newville, M. ATHENA, ARTEMIS, HEPHAESTUS: data analysis for X-ray absorption spectroscopy using IFEFFIT. *J. Synchrotron Radiat.* **12**, 537–541 (2005).
52. Kresse, G. & Furthmüller, J. Efficiency of ab-initio total energy calculations for metals and semiconductors using a plane-wave basis set. *Comput. Mater. Sci.* **6**, 15–50 (1996).
53. Kresse, G. & Furthmüller, J. Efficient iterative schemes for ab initio total-energy calculations using a plane-wave basis set. *Phys. Rev. B* **54**, 11169–11186 (1996).

54. Han, L. et al. Two-in-one template-assisted construction of hollow phosphide nanotubes for electrochemical energy storage. *Inorg. Chem. Front.* **9**, 3398–3411 (2022).
55. Selcuk, S. & Selloni, A. Facet-dependent trapping and dynamics of excess electrons at anatase TiO_2 surfaces and aqueous interfaces. *Nat. Mater.* **15**, 1107–1112 (2016).
56. Perdew, J. P., Burke, K. & Ernzerhof, M. Generalized gradient approximation made simple. *Phys. Rev. Lett.* **77**, 3865–3868 (1996).
57. Si, X. et al. Catalytic production of low-carbon footprint sustainable natural gas. *Nat. Commun.* **13**, 258 (2022).
58. Neese, F. Software update: the ORCA program system, version 4.0. *WIREs Comput. Mol. Sci.* **8**, e1327 (2018).
59. Lu, T. & Chen, F. Multiwfn: a multifunctional wavefunction analyzer. *J. Comput. Chem.* **33**, 580–592 (2012).
60. Humphrey, W., Dalke, A. & Schulten, K. VMD: Visual molecular dynamics. *J. Mol. Graph.* **14**, 33–38 (1996).

Acknowledgements

This work was supported by National Key Research and Development Program of China (2022YFE0107900, 2022YFB3803600 to J.Z.), the National Natural Science Foundation of China (22461142136 to J.Z., 22572051 to S.W.), the Innovation Program of Shanghai Municipal Education Commission (2021-01-07-00-02-E00106 to J.Z.), the Science and Technology Commission of Shanghai Municipality (22230780200, 20DZ2250400, 2018SHZDZX03 to J.Z.), the Chenguang Program of Shanghai Education Development Foundation and Shanghai Municipal Education Commission (24CGA30 to S.W.), and Fundamental Research Funds for the Central Universities (222201717003 to J.Z.). Thanks to the Shanghai Synchrotron Radiation Facility of BL14W1 (https://cstr.cn/31124.02.SSRF. BL14W1) for providing beam time. We thank the staff members of the BL01B beamline (https://cstr.cn/31129.02.NFPS.BL01B) at the National Facility for Protein Science in Shanghai (https://cstr.cn/31129.02.NFPS), for providing technical support and assistance in data collection and analysis.

Author contributions

J.Z., S.W., and C.H. conceived and designed the project. C.H. performed the experiments and analyzed the data. J.Z., S.W. gave suggestions on the research and supervised the project. C.H. performed the theoretical calculations and wrote the manuscript. Z.Y. provided guidance in theoretical calculations. R.Y., C.Z., Y.D., W.C., L.C., and Z.W. conducted part of light-driven experiments. S.W. and J.Z. reviewed the manuscript, and gave suggestions. All authors commented on the manuscript.

Competing interests

The authors declare no competing interests.

Additional information

Supplementary information The online version contains supplementary material available at https://doi.org/10.1038/s41467-026-68429-w.

Correspondence and requests for materials should be addressed to Shiqun Wu or Jinlong Zhang.

Peer review information *Nature Communications* thanks the anonymous reviewer(s) for their contribution to the peer review of this work. [A peer review file is available.]